Int J Adv Manuf Technol (2017) 91:2315–2328
DOI 10.1007/s00170-016-9938-9

ORIGINAL ARTICLE

Developing a self-piercing riveting with flange pipe rivet joining aluminum sheets

Zhichao Huang[1,2] · **Qiuhua Yao**[1,3] · **Jiamei Lai**[4] · **Jingwei Zhao**[2] · **Zhengyi Jiang**[2]

Received: 17 June 2016 / Accepted: 18 December 2016 / Published online: 3 January 2017

Abstract This paper proposes a self-piercing riveting (SPR) method which uses a flange pipe rivet. This joining technology can solve the problems of oblique rivet and incorrect rivet position which are usually found in the SPR with a pipe rivet. The lap shear strength of the joint with a flange pipe rivet is higher than that of a joint with a conventional rivet. In this research, a flange pipe rivet was placed between two sheets with a force applied to the top sheet by a punch riveting machine. The flange pipe rivet moved downward along with the top sheet to induce appropriate bending and form a mechanical interlock in both sheets. Finite element (FE) analysis of the SPR with a flange pipe rivet was done by DEFORM software. The simulated joint cross-section shapes were observed, and the influence of the flange pipe rivet parameters on joint quality was analyzed. Simultaneously, some riveting experiments on joining aluminum sheets were conducted taking into consideration different rivet heights and chamfer angles. The results show that the joining surface is smooth and the simulated joint cross-section shapes are in good agreement with the experimental results. The joining property with a chamfer angle of 45° and a rivet height of 5 mm is found to be the best in joining the Al6063 aluminum alloy sheets with a thickness of 2.4 mm by using the SPR with a flange pipe rivet.

Keywords Self-piercing riveting · Flange pipe rivet · Sheet joining · Finite element analysis · Aluminum

✉ Zhichao Huang
hzc@ecjtu.edu.cn

[1] School of Mechatronics and Vehicle Engineering, East China Jiaotong University, Nanchang, Jiangxi 330013, China

[2] School of Mechanical, Materials and Mechatronic Engineering, University of Wollongong, Northfields Avenue, Wollongong, NSW 2552, Australia

[3] CRRC Zhuzhou Motor Co., Ltd, Zhuzhou, Hunan 412001, China

[4] School of Mechanical and Electrical Engineering, Nanchang University, Nanchang, Jiangxi 330031, China

1 Introduction

The demand for reduction in energy consumption has resulted in the widespread use of lightweight metal alloys, such as magnesium alloys and aluminum alloys, in modern vehicle manufacturing and aerospace manufacturing [1–4]. In practice, light materials used in vehicles are usually joined to achieve weight reduction. Unfortunately, traditional joining technology, such as conventional spot welding, is unable to join light weight materials well [5].

Self-piercing riveting (SPR) is a rapidly developing mechanical joining technique without a prehole. Much research has been done in the numerical simulations and experiments of the SPR process, and the joint quality of SPR [4–9]. The SPR joints possess a higher or similar strength than resistance spot welds [10, 11]. Wang et al. [12] presented a new riveting process driven by gunpowder to form a joint with different geometric characteristics as compared with those joined by the conventional system. Li et al. [13] proposed a hybrid joining process called friction SPR to join low-ductility materials. SPR can join different kinds of material sheets. Mori et al. [14, 15] and Abe et al. [16] have successfully joined aluminum alloy sheets and high strength steel sheets with SPR. He et al. [17, 18] studied the properties of SPR joining copper alloy and aluminum alloy, and joining titanium sheets. Fratini and Ruisi [19] investigated SPR for

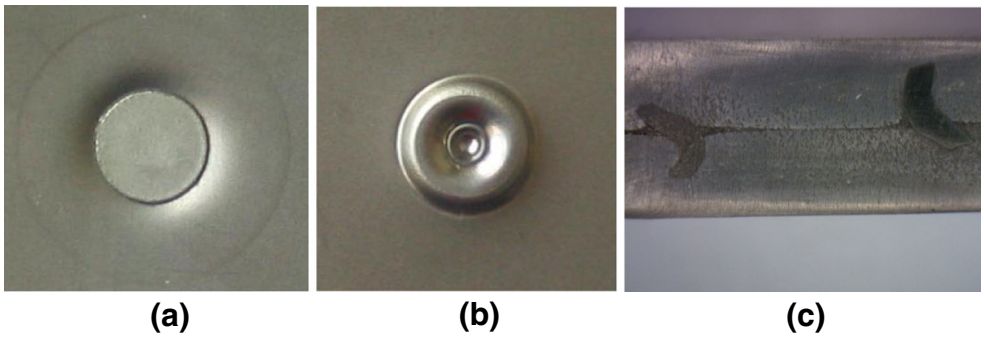

Fig. 1 The *top* (**a**) and *bottom* (**b**) surfaces of an SPR joint and the cross section of an SPR joint with pipe rivet (**c**)

aluminum alloys-composites hybrid joints. Wagner et al. [20] investigated damage propagation around rivets in multiple joined carbon fiber reinforced plastics-steel structures due to loads as a consequence of different coefficients of thermal expansion. There have been some papers about the static and fatigue behavior of SPR. Fu and Mallick [21], Kang and Kim [22], Zhao et al. [23], and Xing et al. [24] studied the fatigue behavior of self-piercing riveted joints of aluminum alloy. Huang et al. [25] investigated the fatigue behavior of self-piercing riveted joints of aluminum alloy and steel sheets. Mori et al. [26], Su et al. [27], and Xing et al. [28] compared the fatigue response of self-piercing rivets and clinch joints.

Kato et al. [29] proposed a new type of SPR with a pipe rivet. Huang et al. [30] discussed finite element simulation results of riveting with a pipe rivet using DEFORM-2D software. In those studies, some rivets with different correlation angles were made and used in the experiments. The pipe rivet is oblique and instable in the joint. Huang et al. [31] proposed a new method of SPR with inner flange pipe rivet joining Al6063 aluminum alloy sheets. SPRs with solid rivet were studied, and they are unsmooth on the top and bottom surfaces of joints [32].

Currently, the existing publications are mainly focused on SPR. A circle mark usually exists at the top surface of SPR, and the bottom surface is convex, as shown in Fig. 1a, b. As a result, the SPR method is usually used in joining metal sheets for applications in rear door inner subassembly. SPR with a pipe rivet has a flat top surface, but there can be problems of oblique rivet and incorrect rivet position, as shown in Fig. 1c.

In this paper, an SPR method using a flange pipe rivet is proposed, as shown in Fig. 2. Unlike a conventional rivet which has a flange at one end of the rivet and has a prehole in sheets, as shown in Fig. 3, the flange rivet has a flange in the middle of the rivet. During the joining process, the flange rivet penetrates into the sheets and deforms into two crescent shapes from both ends. Compared with conventional riveting SPR and SPR with a pipe rivet, SPR with a flange pipe rivet has a number of advantages. (1) No predrilled or prepunched holes are required; (2) there is no need for exact alignment between the sheets being joined and the rivet setting machine; (3) there is reduced risk of the rivet wall buckling; (4) there is enhanced precision of the rivet position due to the function of the rivet; (5) there is no need for complex die; and (6) the joints are stronger due to the mechanical interlocks formed by both ends of the rivet.

In this paper, an SPR joining process is developed for joining aluminum sheet material Al6063. Numerical simulation is conducted to determine the design of the SPR. The designed SPR and joining process are further validated by experiments.

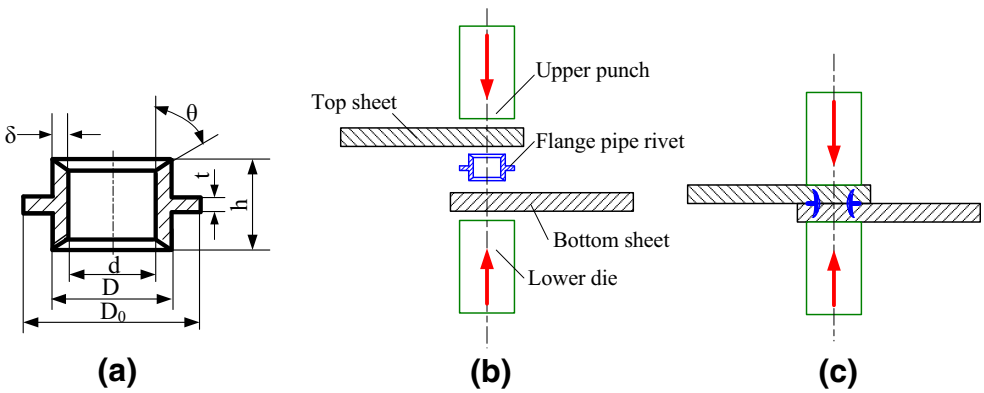

Fig. 2 Principle of SPR with a flange pipe rivet: **a** main geometric parameters of the flange pipe rivet, **b** riveting process with the flange pipe rivet, and **c** cross-section shape of the joint

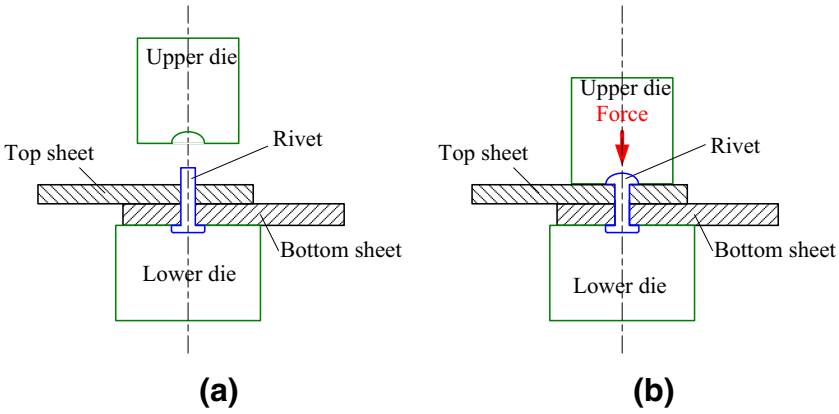

Fig. 3 Schematic of conventional riveting: **a** before riveting and **b** after riveting

2 Numerical simulations of the riveting process

Numerical analysis drastically saves development time, shows the best way to conduct the experiment, and thereby improves the project [33]. The joining process was modeled by using DEFORM finite element (FE) software. The upper punch and lower die were thought to be rigid bodies, while sheets and SPR were regarded as plastic bodies with axially symmetric elements. The Newton-Raphson method was used for simulations.

2.1 Geometric model

The main dimensions of the rivet include height h, thickness δ, chamfer angle θ, outer diameter D, inner diameter d, outer diameter of flange D_0, and flange thickness t, as shown in Figs. 2a and 4. In order to increase the joining strength, the inner corners of the rivet ends are machined in chamfer shape in advance, and both ends of the rivet are made to expand in two metal sheets and to form a crescent shape. The rivets are made of stainless steel SUS304 with different angles ($\theta = 30°$, 45°, 60°, and 90°) and heights (h = 4 and 5 mm). Both the upper and bottom sheets are aluminum Al6063 sheets with a 2.4-mm thickness.

A 2D axisymmetric model was generated in the commercial FE code DEFORM using four-node elements, as shown in Fig. 5.

2.2 Material model

The material properties of the sheets and the rivet are shown in Table 1. The rivet is made of stainless steel 304 (SUS304), and the sheets are made of aluminum alloy Al6063. The flange pipe rivet has not only hardness to piece sheets but also ductility to spread both rivet ends in the sheets. The ends of the flange pipe rivet pierced both sheets, and the shear deformation energy per unit volume in sheet reached a certain value, and then plastic deformation occurred.

The flow stress equation for aluminum alloy Al6063 and stainless steel 304 used in the simulations is given with a constitutive model:

$$\overline{\sigma} = f\left(\overline{\varepsilon}, \dot{\overline{\varepsilon}}, T\right) \tag{1}$$

where $\overline{\sigma}$ is the effective stress, $\overline{\varepsilon}$ is the effective strain, $\dot{\overline{\varepsilon}}$ is the effective strain rate, and T is the temperature. The experiments were conducted at room temperature. The material data was

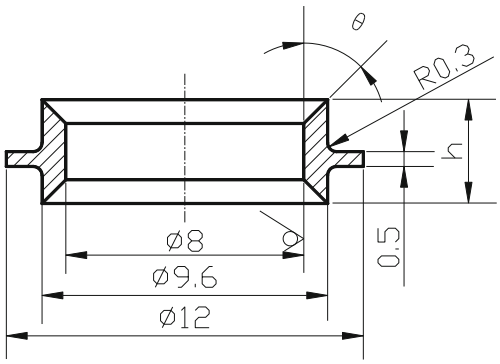

Fig. 4 Size of flange pipe rivet

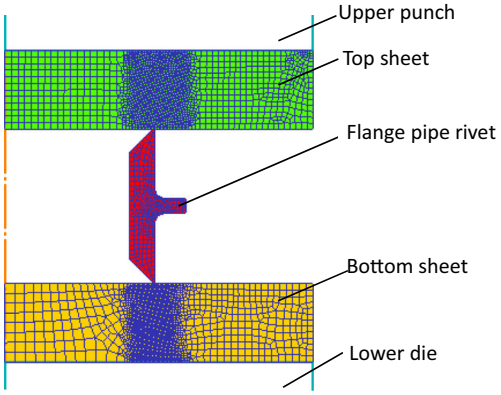

Fig. 5 Finite element model and initial meshes

Table 1 Mechanical properties of the sheets and the rivet

Materials	Young's modulus (GPa)	Poisson's ratio	Yield strength (MPa)	Ultimate strength (MPa)
Al6063	68.9	0.33	80	173
SUS304	210	0.3	510	1000

obtained from material database in DEFORM 2D. The curves of flow stress-strain are shown in Fig. 6.

When the rivet penetration depth is increased, cracks occur at the tip of the rivet where the sheet metal has undergone large shearing deformation. In this study, the Normalized Cockcroft & Latham expression was used as the ductile fracture criterion [34]:

$$\int_0^{\varepsilon_f} \left(\frac{\sigma_{\max}}{\overline{\sigma}} \right) d\overline{\varepsilon} = C \tag{2}$$

where ε_f is the equivalent fracture strain, $\sigma_{\max}$ is the maximum principal stress, $\overline{\sigma}$ is the equivalent stress, $\overline{\varepsilon}$ is the equivalent strain, and C is the damage value of the material. The damage value was evaluated by a tensile test and defined as a sheet material constant. The fracture criterion of the penetration initiation of Al6063 is Normalized Cockcroft & Latham, and the critical value is determined as 0.05 by a tensile test [35].

2.3 Meshing parameters

A quadrilateral element was used for the numerical modeling. The defined mesh density window is shown in Fig. 7. The mesh density window will move with the top sheet during deformation. This area has a mesh density definition applied to it and will cause the area to be meshed with an appropriate mesh density. The 4 points make up the mesh density window.

In the upper sheet, the relative movement size is 0.1 for Window 1, 0.5 for Window 2, and 1 for Window 3. The velocity of Windows 1, 2, and 3 is 0 mm/s. The number of elements is about 2000, and the size ratio is 3.

In the lower sheet, the relative movement size is 0.1 for Window 1, 0.5 for Window 2, and 1 for Window 3. The velocity of Windows 1, 2, and 3 is 0 mm/s. The number of elements is about 2000, and the size ratio is 3.

In flange pipe rivet, the number of elements is about 300, and the size ratio is 3.

Automatic remeshing is the most convenient way to handle the remeshing of objects undergoing large plastic deformation. The slave surface of the sheets does not penetrate the master rigid die and punch, but the flange pipe rivet may penetrate the surface of the sheets. If any part of a master object penetrates a slave object beyond the depth specified under maximum interference depth, remeshing will be triggered. The maximum interference depth is 0.02 mm in the simulation. During simulation, the object will be remeshed when the remeshing criteria have been fulfilled or the mesh becomes unusable. Then, the solution information from the old mesh is interpolated onto the new mesh, and the simulation continues.

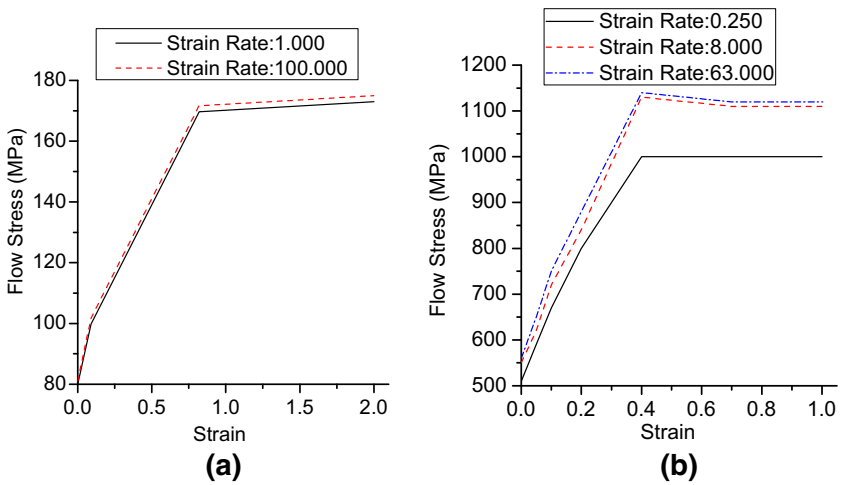

Fig. 6 Mechanical properties of **a** Al6063 and **b** SUS304

Fig. 7 Meshes of the simulation

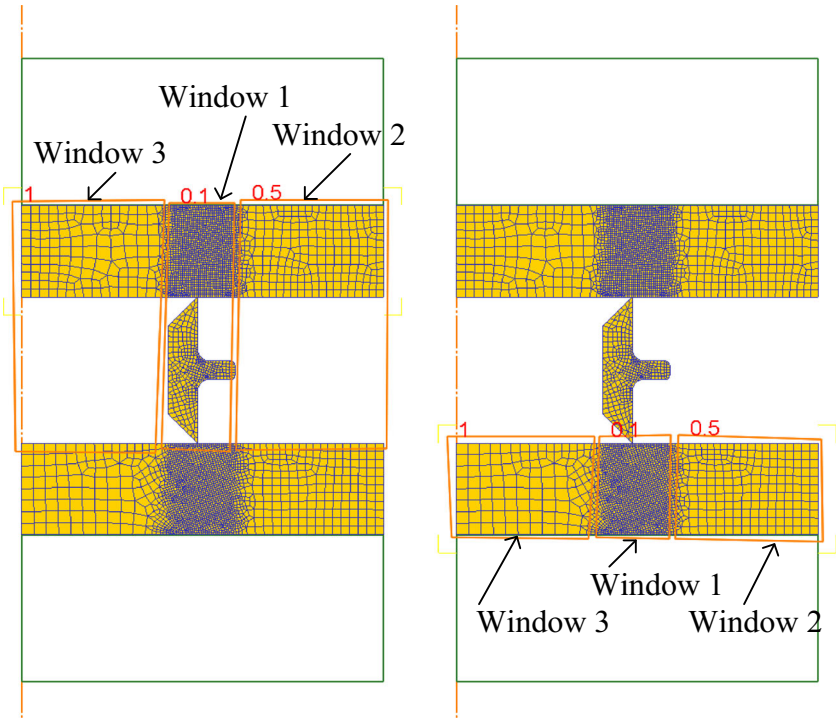

2.4 Boundary conditions

In the simulation, a friction model was considered using the Coulomb friction law [36], as follows:

$$\tau_f = \mu\sigma_n \tag{3}$$

where τ_f is the friction shear stress (MPa), σ_n is the stress (MPa), and μ is the friction coefficient. Table 2 shows the values of the friction coefficient at the interface between the different parts in the simulations. These values were obtained from inverse analysis using one joint as reference and kept constant for all the simulations [37].

The maximum displacement for any node should not exceed one third the length of its element edge length in one step. In this simulation, the minimum length of its element edge length is 0.06 mm, so the step is 0.02 mm and the number of simulation steps is 250. The deformable bodies are the rivet and the aluminum sheets. The speed of the punch was set to 20 mm/s.

Table 2 Friction coefficients at the interface between the different parts

Master (part 1)	Slave (part 2)	Friction coefficient
Rivet	Top sheet	0.1
Rivet	Bottom sheet	0.1
Upper punch	Top sheet	0.08
Lower die	Bottom sheet	0.08
Top sheet	Bottom sheet	0.08

2.5 Numerical analysis and discussion

The arrangement of operating sequence is shown in Table 3. The deforming shapes of sheets and flange pipe rivet (FF2) obtained from the simulation are shown in Fig. 8, and S is the punch stroke. A mechanical interlock between the two sheets is formed. The flange on the pipe-wall of the rivet can eliminate joining defects including oblique and incorrect positioning of the rivet during the riveting process. The riveting process with the flange pipe rivet is like the SPR riveting process [1]. In the first step, the flange pipe

Table 3 Arrangement of operating sequence with different angles and heights

No.	Section labels	Rivet parameters		Icon of pictures
		Chamfer angles (°)	Height (mm)	
1	FT1	30	4	Fig. 9a
2	FT2	30	5	Fig. 9b
3	FF1	45	4	Fig. 9c
4	FF3	45	4.5	Fig. 9d
5	FF2	45	5	Fig. 9e
6	FF4	45	5.5	Fig. 9f
7	FS1	60	4	Fig. 9g
8	FS2	60	5	Fig. 9h
9	FN1	90	4	Fig. 9i
10	FN2	90	5	Fig. 9j

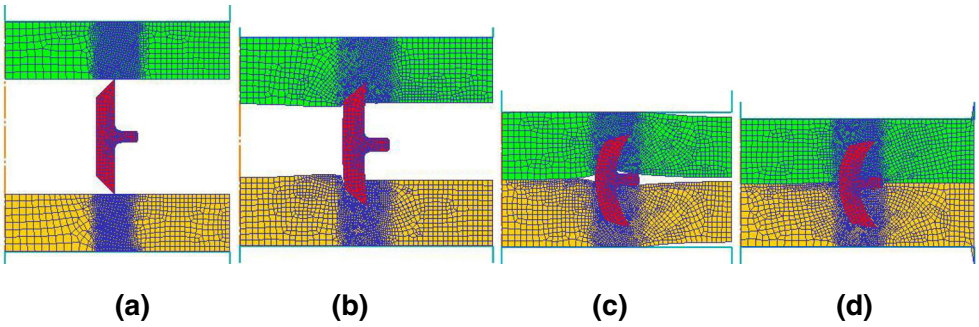

Fig. 8 Deforming shapes of sheets and rivet obtained from the simulation: **a** clamping, $S = 0.0$ mm, **b** piercing, $S = 2.2$ mm, **c** flaring, $S = 4.2$ mm, and **d** compression, $S = 5.0$ mm

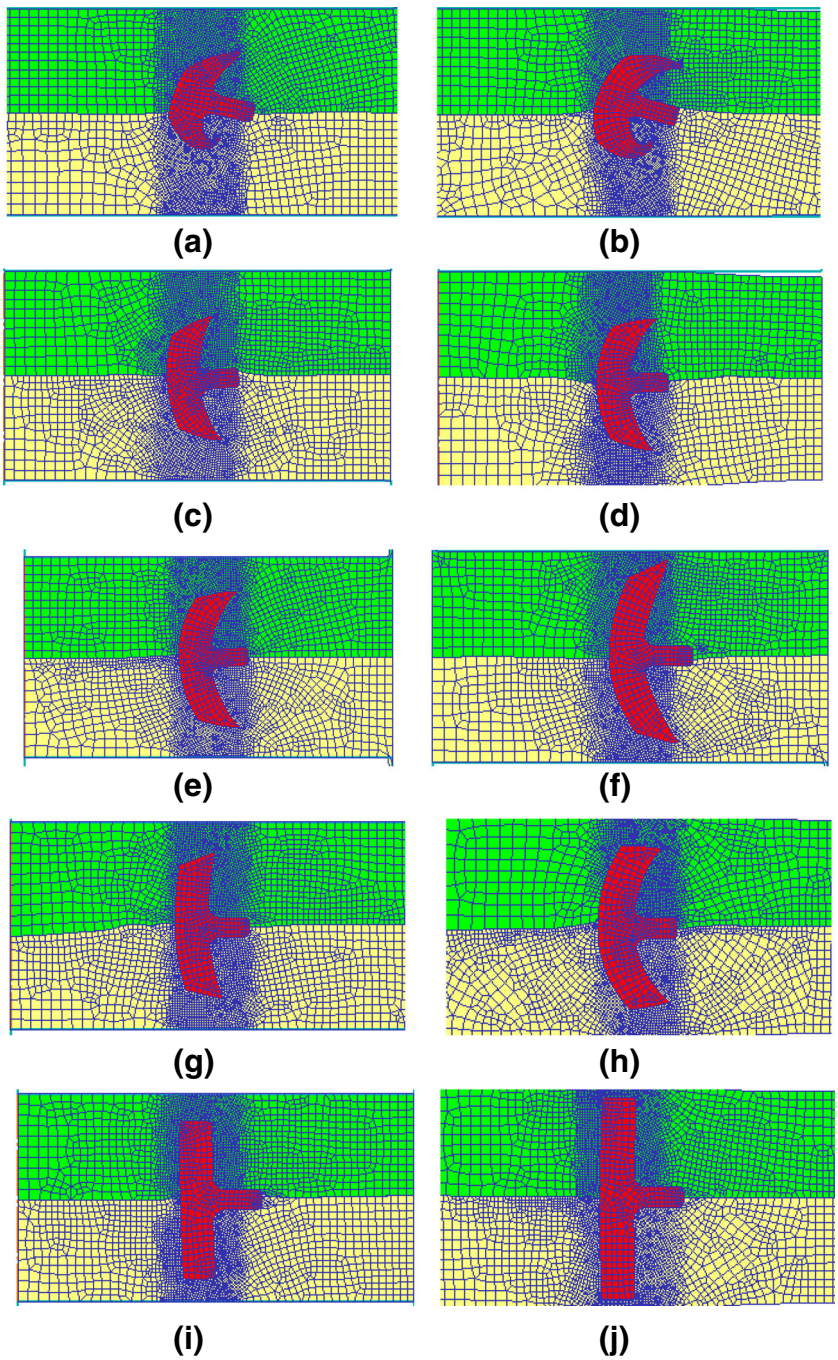

Fig. 9 Comparison of every group numerical simulation: **a** FT1, **b** FT2, **c** FF1, **d** FF3, **e** FF2, **f** FF4, **g** FS1, **h** FS2, **i** FN1, and **j** FN2

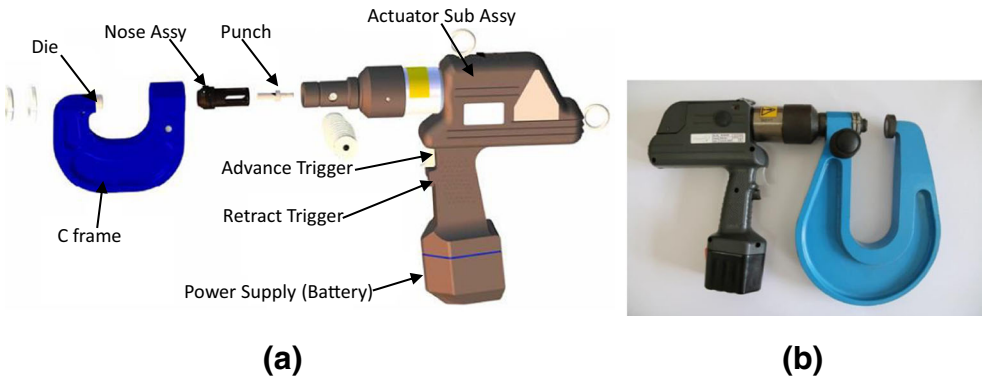

Fig. 10 Hand-held self-piercing riveting machine: **a** exploded view and **b** assembled view

rivet is placed between two aluminum alloy sheets and pressed by a punch. In the second step, both sheets undergo a severe deformation because the hardness and strength of the material of the rivet are superior to those of the sheets. In the third step, the chamfer angle and flange of the rivet act on the pierced rivet. Both ends of the flange pipe rivet start to flare inside the sheets and form a crescent shape, and a mechanical interlock is formed. It can enhance the joint quality and strength. Finally, the punch continues the stroke and stops when a scheduled force or stoke is reached.

The cross-sectional shapes of the finite element simulation of riveting with different angles and heights are shown in Fig. 9a–j, respectively. The following observations can be drawn:

1. When the chamfer angle $\theta = 30°$, the ends of the rivet are too sharp. Rivet bend deformation is too large after penetrating into sheets and rolling up around the flange. The pierced depth is not enough and easy to drop.
2. When the chamfer angle $\theta = 45°$, as the punching continues, both ends of the flange pipe rivet which is set between the upper and the lower sheets penetrate into both sheets. Sheet materials flow smoothly around the ends of the rivet, inducing decreased deformation resistance on the chamfer. This ensures that the rivet deforms appropriately and pierces well into the sheets. The best chamfer angle is $\theta = 45°$ for obtaining improved cross-section shape based on the finite element simulation of riveting. Finite element simulations of riveting with the chamfer angle of $\theta = 45°$ and heights of $h = 4$, 4.5, 5, and 5.5 mm were done.
3. When the chamfer angle $\theta = 60°$, sheet materials have a little difficulty in flowing around the ends of the rivet as the punching progresses.
4. When the chamfer angle $\theta = 90°$, the sheet materials have difficulty in flowing around the ends of the rivet as punching continues. As a result, the rivet does not experience bending deformation and pierces perpendicularly into sheets, as shown in Fig. 9i, j. The bear loads of joints are decreased during the tensile test due to the lack of mechanical interlock.
5. The deformation characteristics of a self-piercing riveted joint reflect the quality of the joint. The higher the value of the height of the flanged pipe rivet, the deeper the flanged pipe rivet pierces into both sheets. The tip of the flanged pipe rivet was also close to the surface of both sheets. The pierced depth was not enough and the mechanical interlock was worse because the value of the height of the rivet was small (Fig. 9a). The procedure that was used to assess the quality of a self-piercing riveted joint involved measurement of the distance between the tip of the rivet and the surface of the pierced sheets and the mechanical interlock. Those two criteria were interconnected in that a too low or too high flanged pipe rivet could result in a worse mechanical interlock. The results indicate that the pierced depth and the mechanical interlock are better when the height of the flanged pipe rivet is 5 mm.

Fig. 11 Picture of flange pipe rivet

The finite element simulations show that the best optimal design parameters are chamfer angle $\theta = 45°$ and rivet height $h = 5$ mm.

3 Experimental setup

3.1 Experimental equipment

The SPR with a flange pipe rivet was done using Henrob's RV300028 SPR machine, as shown in Fig. 10. The lower die is flat. The shape and size of the rivet are shown in Figs. 4. and 11.

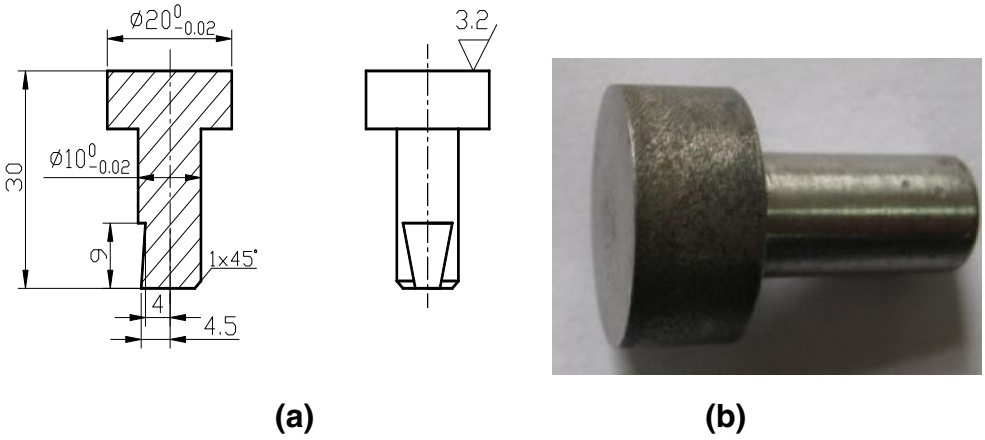

Fig. 12 Dimensions of the lower die: **a** figure in CAD of lower die and **b** picture of lower die after heat treatment

The material of the rivets is austenitic stainless steel 304. The height of the rivet is 4 or 5 mm. Four kinds of chamfer angle θ (30°, 45°, 60°, and 90°) at both ends of the rivet were used in the experiments. The material of the lower die is high-quality carbon tool steel T10A, and the dimensions of the die are shown in Fig. 12. The top of the die is flat, which is beneficial for riveting.

3.2 Experimental procedure

After installing the lower die, the bottom sheet is put on the lower die. The flange pipe rivet is fed directly upon the bottom sheet surface, and then another sheet is put on the rivet. The installation sequences are shown in Fig. 13a. The riveting process is shown in Fig. 13b, and the top and bottom surfaces of the joint are shown in Fig. 13c, d. It can be seen that the joining surface is smooth. The cross shapes of joints formed by four different chamfer angles (30°, 45°, 60°, 90°) and two different heights (4 and 5 mm) are shown in Fig. 14a–h.

The joint samples were sectioned and macro-inspection was carried out in order to measure the remaining material thickness and the bending angle by a hand-held digital microscope.

4 Comparison between experimental results and simulation results

Figure 14a–h compares the simulation results with the real sections of the joint under different levels of angle θ and height h. The comparison shows a good geometric correlation.

The cross-sectional shapes joining two sheets obtained by simulations are compared with those of experiments. It can be seen that the cross-sectional shapes of simulations are in good agreement with the experimental ones. As shown in Fig. 14, the

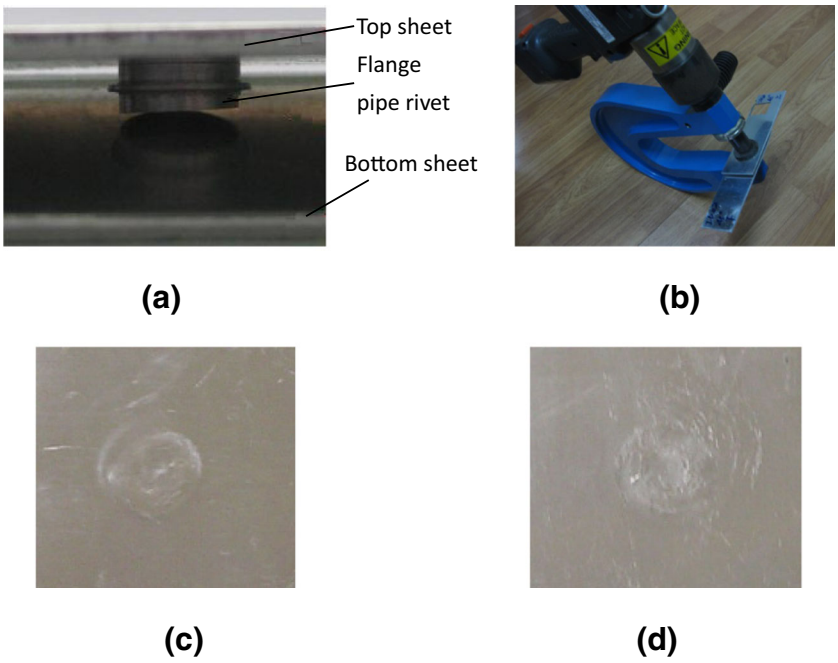

Fig. 13 The experiment of SPR with a flange pipe rivet: **a** macro scope of the sequence, **b** process of riveting, **c** *top surface* of the joint, and **d** *bottom surface* of the joint

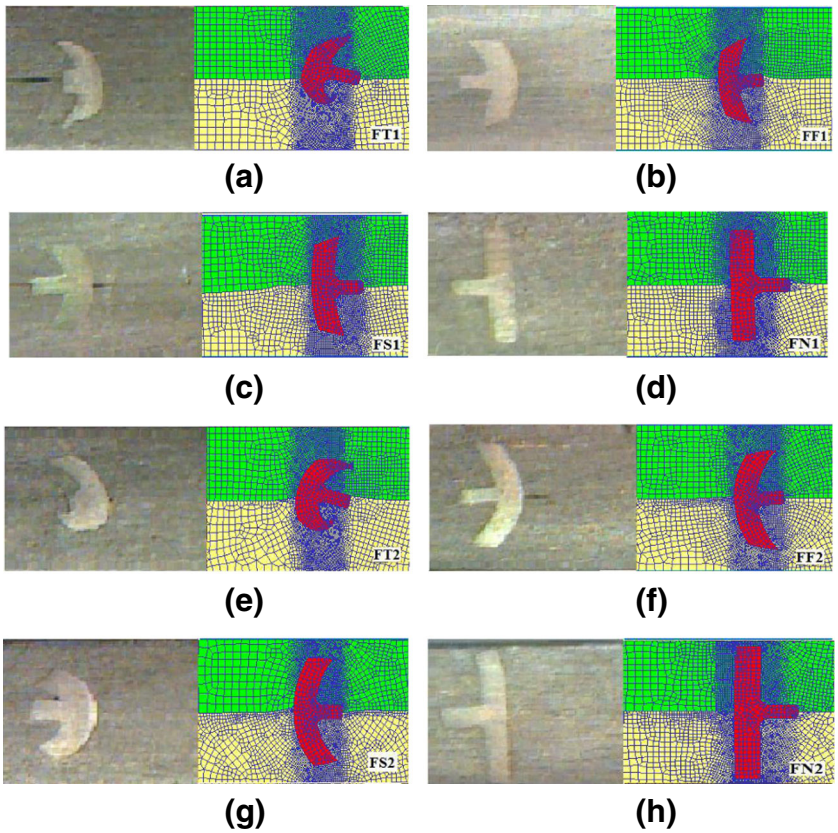

Fig. 14 Comparison of cross-sectional shapes of rivet and sheets between the simulations and the experiments. **a** $\theta = 30°$, $h = 4$ mm, **b** $\theta = 45°$, $h = 4$ mm, **c** $\theta = 60°$, $h = 4$ mm, **d** $\theta = 90°$, $h = 4$ mm, **e** $\theta = 30°$, $h = 5$ mm, **f** $\theta = 45°$, $h = 5$ mm, **g** $\theta = 60°$, $h = 5$ mm, and **h** $\theta = 90°$, $h = 5$ mm

appropriate bending deformation of the rivet occurs at 45° and 60°, and it almost does not occur at 90°, but occurs severely at 30°.

The flange pipe rivet can solve the problems of oblique rivet and incorrect rivet position which are usually found in SPR with a pipe rivet.

5 Mechanical properties

5.1 Tensile tests procedure

Tensile tests were conducted to evaluate the mechanical properties of the joints with different chamfer angles of 30°, 45°, 60°, and 90° and heights of 4, 4.5, 5, and 5.5 mm. Lap-shear specimens are the most common style of sheet connection. The detailed lap-shear specimen geometries are illustrated in Fig. 15.

Static strength tensile test for lap-shear specimens is performed on a tensile testing machine AG-250KN2SMD with a loading rate of 2 N/s (Fig. 16a). The tensile processes of lap-shear specimens are shown in Fig. 16b. The data of load and displacement are collected by transducers to a sampling device installed on a PC.

5.2 Tensile properties

In the static strength tests, when the riveting joint is destroyed, the peak load will act as the static strength. Figure 17 shows the static load versus displacement curves. These tests are carried out with rivet heights of 4 and 5 mm, chamfer angles

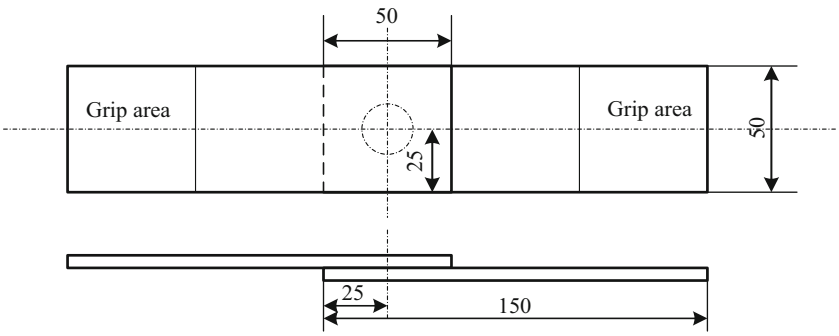

Fig. 15 Geometry of the lap-shear specimen

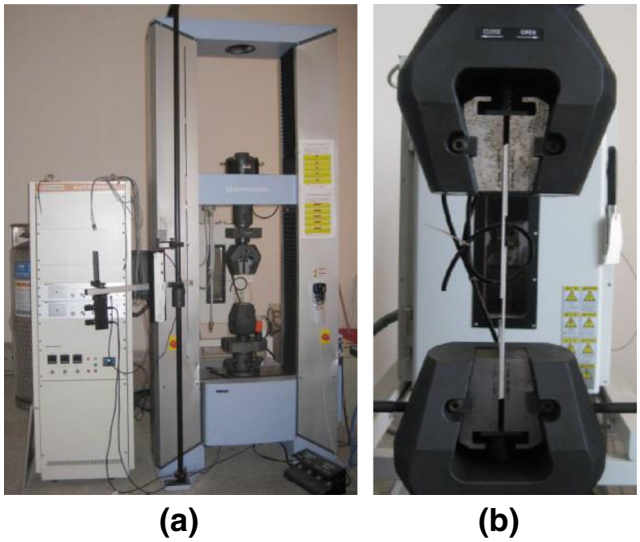

Fig. 16 Configuration: **a** tensile tester and **b** tensile test of lap-shear specimens

of 30°, 45°, 60°, and 90°, and an aluminum alloy sheet thickness of 2.4 mm, and other rivet parameters are the same. The tensile strength of the joints is quite different because it changes along with the chamfer angle and height.

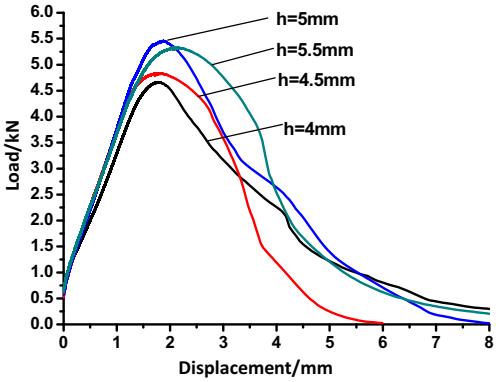

Fig. 18 Lap-shear strength comparison for different height rivets

The joints with $\theta = 45°$ exhibit the highest peak loads under a certain value of h, and also the joint with $h = 5$ mm shows a higher peak load as compared to that with $h = 4$ mm when $\theta = 45°$. When θ increases from 45° to 90°, the peak load decreases gradually. Under a given value of h, the joint with $\theta = 30°$ shows the minimum peak load due to the highly

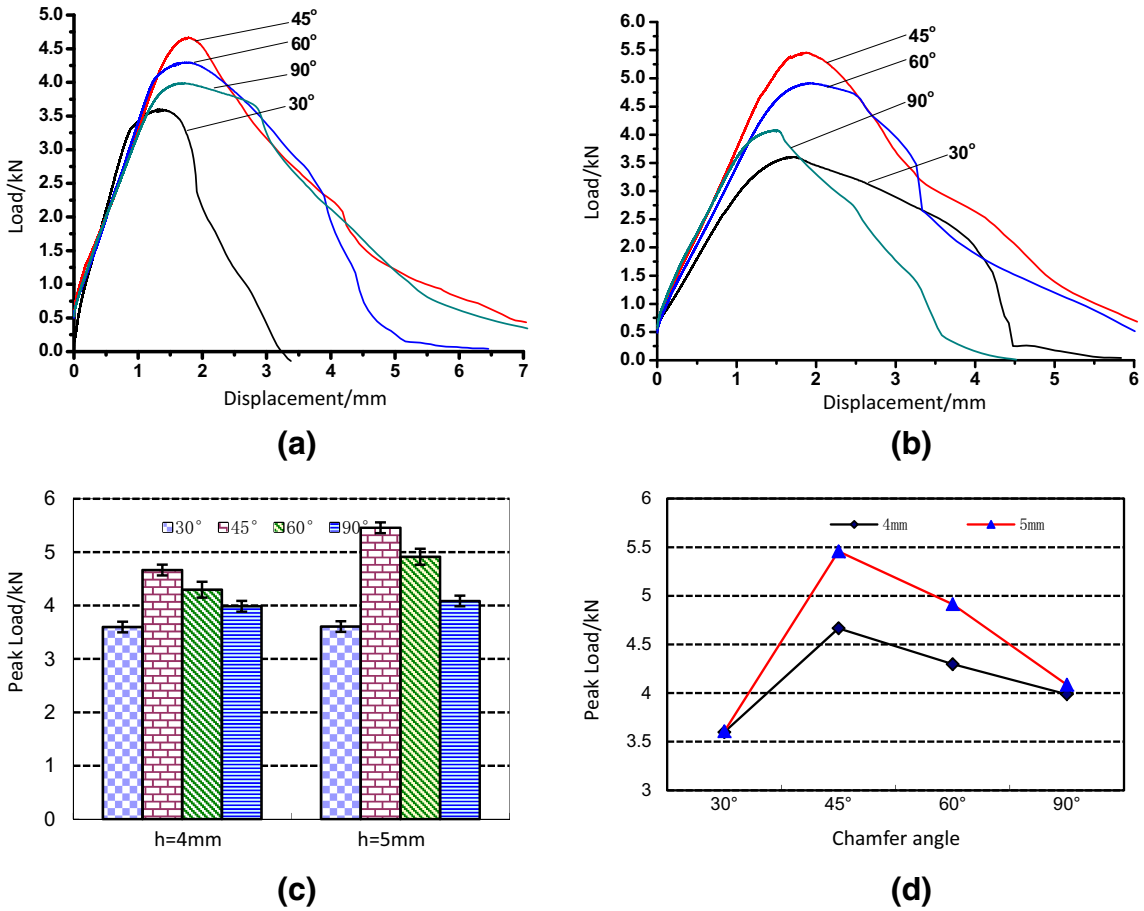

Fig. 17 Joining strength comparison for different chamfers: **a** $h = 4$ mm, **b** $h = 5$ mm, **c** joint strength comparison for shear sample, and **d** joint strength comparison for shear samples

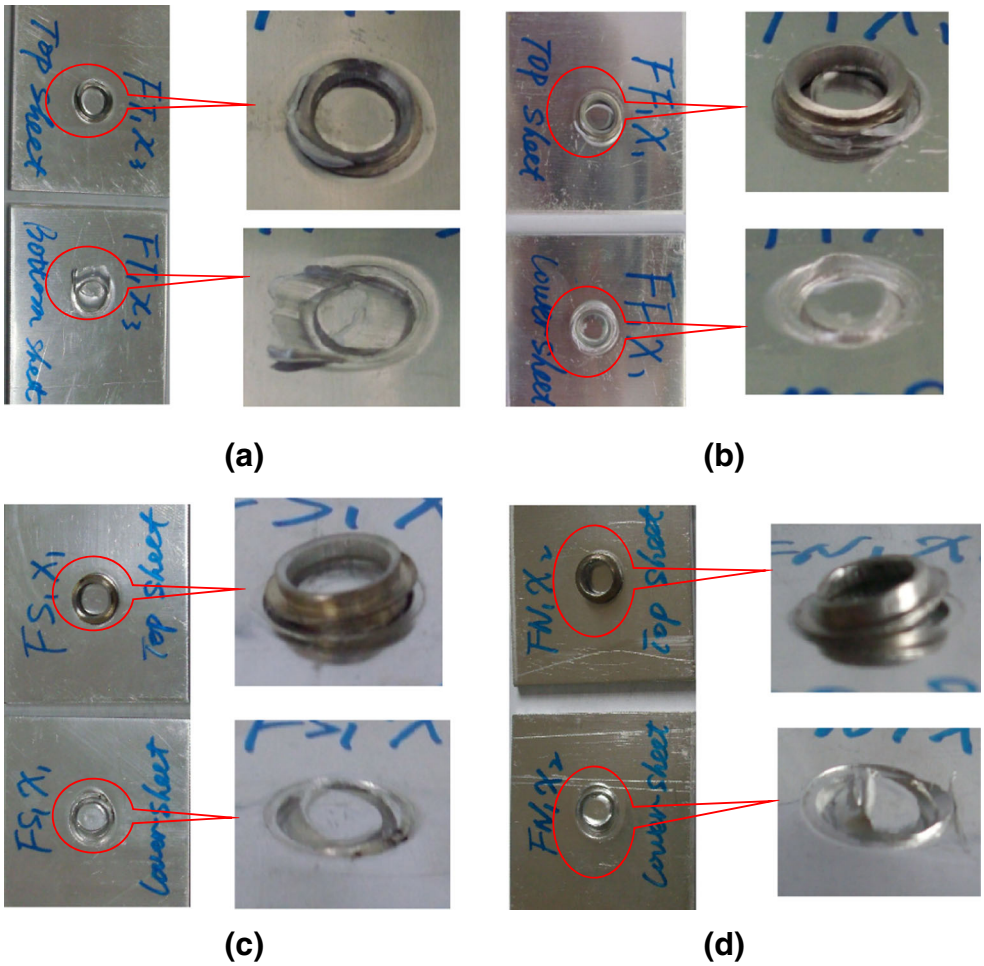

Fig. 19 Failure modes occurred among four kinds of chamfer during lap-shear test: **a** $\theta = 30°$, **b** $\theta = 45°$, **c** $\theta = 60°$, and **d** $\theta = 90°$

bending deformation which causes limited piercing of the rivet into sheets.

Both the upper and bottom sheets are aluminum Al6063 sheets with 2.4-mm thickness. The rivets are made of stainless steel SUS304 with 45° angles which have the best joining property. Figure 18 shows the curves of load versus displacement from lap shear tests. The tensile strength of joints changes along with the height. In lap-shear tests, the samples

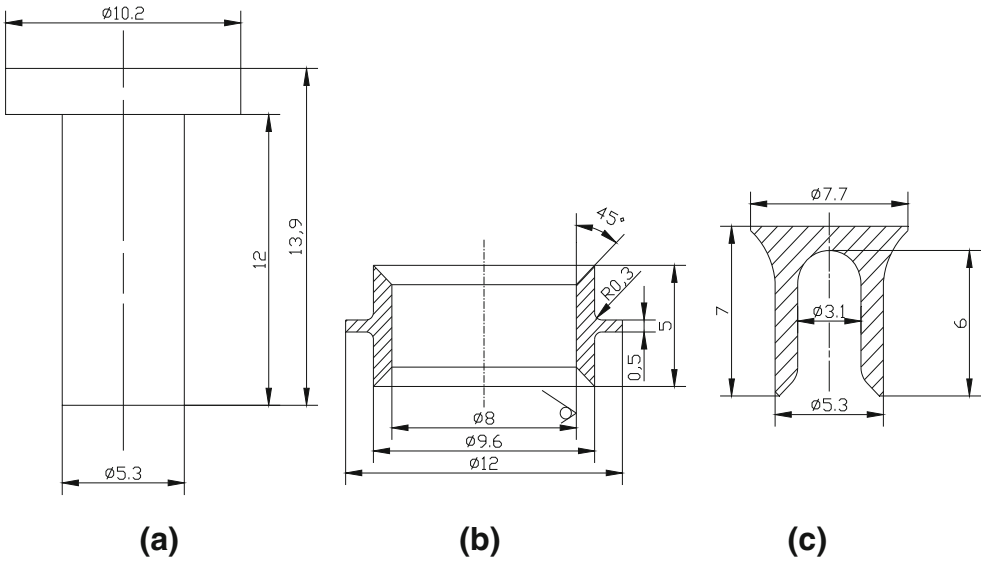

Fig. 20 Dimensions of **a** conventional rivet, **b** flange pipe rivet, and **c** self-piercing rivet

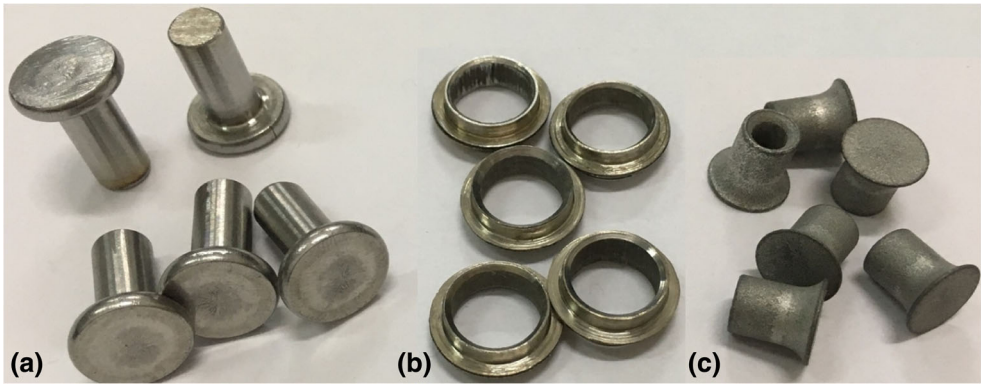

Fig. 21 Pictures of **a** conventional rivet, **b** flange pipe rivet, and **c** self-piercing rivet

(h = 5 mm) exhibited the highest strength of the four different rivet heights, while the joint with the rivet height (4 mm) exhibited the worst behavior. It is seen from Fig. 18 that the maximum load which the riveting joint could bear increased along with the increasing of rivet height, and the load declined after reaching the peak. When the height is 5 mm, the peak load that riveting specimens could bear reached maximum value and good mechanical property was obtained.

When sheet thickness is 2.4 mm + 2.4 mm, the rivet height is 5 mm which is slightly bigger than the thickness sum of two layers of sheets. Compared with the two layers of sheets with 2.4 mm + 2.4 mm, the rivet height of 4 and 4.5 mm is less than the sum of sheet thickness. The embedded depth of the rivet into the sheet after expansion deformation is not large enough, and this resulted in the reduction of the load that the riveting specimen could bear in the tensile test. When the rivet height is 5.5 mm, which is bigger than the sum of thickness of the two layers of the sheet, the surpass dimension accounted for 14.58% of the sheet thickness. In this case, both ends of rivet would easily get close to the sheet surface, meaning that the surface material could be pulled out and form a through-hole in the tensile test which led to the reduction of the riveting specimen's mechanical property.

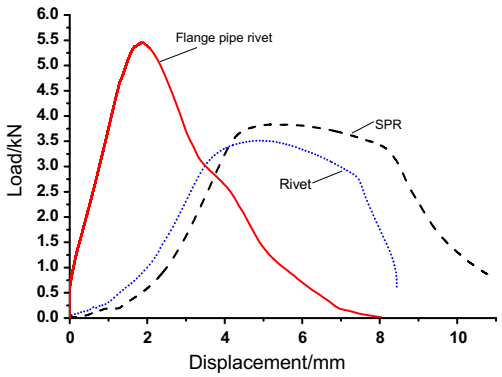

Fig. 22 Load–displacement curves of lap shear tests with a conventional rivet, an SPR, and a flange pipe rivet

5.3 Failure mode

The shear strength of lap-shear specimens depends on several factors including the tensile strength, shear strength, and deformation of the pierced rivet. The important influence factors can be obtained through analysis of the failure models. Figure 19 shows the morphology of the specimens after failure. It can be seen that the failure mode is the same under all the conditions. The deformed rivets are pulled out from the bottom sheet. The mechanical interlock between deformed rivets and sheets dominates the strength of the joints. If the rivet is deformed with the formation of a good mechanical interlock, then the joint quality will be improved.

6 Comparison of flange pipe rivet with conventional rivet and SPR

The conventional rivet and flange pipe rivet are made of SUS304 stainless steel, and the self-piercing rivet is made of 36MnB4 high strength steel. The dimensions of the conventional rivet, flange pipe rivet, and self-piercing rivet are shown in Fig. 20. The cross-sectional area of the flange pipe rivet is the same as that of a conventional rivet. The pictures of rivets are shown in Fig. 21.

The load–displacement curves of lap shear tests joining two 2.4-mm aluminum sheets with a conventional rivet, an SPR, and a flange pipe rivet are shown in Fig. 22. The maximum load is 3513 N for the conventional rivet, 5457 N for the flange pipe rivet, and 3833 N for the self-piercing rivet. The results show that the lap shear strength of joints with the flange pipe rivet is the highest.

7 Conclusion

The mechanisms of joining the Al6063 sheets by SPR with a flange pipe rivet have been studied by numerical and

experimental investigations. The joining method can be used in joining other materials.

1. The results of simulations and experiments indicate that the SPR with a flange pipe rivet is practicable for joining aluminum sheets with smoother joining surface than an SPR and a conventional rivet, reducing the risk of the rivet wall buckling with no need for complex die.
2. There is no predrilled or prepunched hole required for SPR with a flange pipe rivet, and no need for exact alignment between the sheets being joined and the rivet setting machine.
3. The joining technology proposed in the present study can solve the problems of oblique rivet and incorrect rivet position which are usually found in SPR with a pipe rivet.
4. Factors including chamfer angle and rivet height that influence SPR are analyzed. The chamfer angle is found to dominate the deformation during the riveting process.
5. The joining property with a chamfer angle of 45° and a rivet height of 5 mm is found to be the best for joining Al6063 aluminum alloy sheets with a thickness of 2.4 mm by using the SPR with a flange pipe rivet.
6. The lap-shear joint strength of SPR with a flange pipe rivet increased due to the mechanical interlocks formed by both ends of the rivet.

Acknowledgements This research is supported by the National Natural Science Foundation of China (51265012) and (51565014), Ganpo excellence 555 engineering talents of Jiangxi Province. The authors would like to thank Dr. Madeleine Strong Cincotta at the University of Wollongong for assisting in the English language editing.

References

1. Atzeni E, Ippolito R, Settineri L (2009) Experimental and numerical appraisal of self-piercing riveting. CIRP Ann - Manuf Technol 58:17–20
2. Cai W, Wang PC, Yang W (2005) Assembly dimensional prediction for self-piercing riveted aluminum panels. Int J Mach Tools Manuf 45:695–704
3. He X, Pearson I, Young K (2008) Self-pierce riveting for sheet materials: state of the art. J Mater Process Technol 199:27–36
4. He X, Gu F, Ball A (2012) Recent development in finite element analysis of self-piercing riveted joints. Int J Adv Manuf Technol 58: 643–649
5. He X, Xing B, Zeng K, Gu F, Ball A (2013) Numerical and experimental investigations of self-piercing riveting. Int J Adv Manuf Technol 69:715–721
6. Porcaro R, Hanssen AG, Langseth M, Aalberg A (2006) Self-piercing riveting process: an experimental and numerical investigation. J Mater Process Technol 171:10–20
7. Li D, Han L, Thornton M, Shergold M (2012) Influence of edge distance on quality and static behaviour of self-piercing riveted aluminium joints. Mater Des 34:22–31
8. Haque R, Williams NS, Blacket SE, Durandet Y (2015) A simple but effective model for characterizing SPR joints in steel sheet. J Mater Process Technol 223:225–231
9. Hoang NH, Porcaro R, Langseth M, Hanssen AG (2010) Self-piercing riveting connections using aluminium rivets. Int J Solids Struct 47:427–439
10. Kim DW, Xu J, Li W, Blake D (2006) Force characteristics of self-piercing riveting. Proc Inst Mech Eng Part B J Eng Manuf 220: 1259–1266
11. Han L, Thornton M, Shergold M (2010) A comparison of the mechanical behaviour of self-piercing riveted and resistance spot welded aluminium sheets for the automotive industry. Mater Des 31:1457–1467
12. Wang B, Hao C, Zhang J, Zhang H (2006) A new self-piercing riveting process and strength evaluation. J Manuf Sci Eng 128:580
13. Li Y, Wei Z, Wang Z, Li Y (2013) Friction self-piercing riveting of aluminum alloy AA6061-T6 to magnesium alloy AZ31B. J Manuf Sci Eng 135:061007-1-7
14. Mori K, Kato T, Abe Y, Ravshanbek Y (2006) Plastic joining of ultra high strength steel and aluminium alloy sheets by self piercing rivet. CIRP Ann - Manuf Technol 55:283–286
15. Mori K, Abe Y, Kato T (2014) Self-pierce riveting of multiple steel and aluminium alloy sheets. J Mater Process Technol 214:2002–2008
16. Abe Y, Kato T, Mori K (2009) Self-piercing riveting of high tensile strength steel and aluminium alloy sheets using conventional rivet and die. J Mater Process Technol 209:3914–3922
17. He X, Zhao L, Deng C, Xing B, Gu F, Ball A (2015) Self-piercing riveting of similar and dissimilar metal sheets of aluminum alloy and copper alloy. Mater Des 65:923–933
18. He X, Wang Y, Lu Y, Zeng K, Gu F, Ball A (2015) Self-piercing riveting of similar and dissimilar titanium sheet materials. Int J Adv Manuf Technol 80:2105–2115
19. Fratini L, Ruisi VF (2009) Self-piercing riveting for aluminum alloys-composites hybrid joints. Int J Adv Manuf Technol 43(1–2):61–66
20. Wagner J, Wilhelm M, Baier H, Fssel U, Richter T (2014) Experimental analysis of damage propagation in riveted CFRP-steel structures by thermal loads. Int J Adv Manuf Technol 75(5–8):1103–1113
21. Fu M, Mallick PK (2003) Fatigue of self-piercing riveted joints in aluminum alloy 6111. Int J Fatigue 25:183–189
22. Kang SH, Kim HK (2015) Fatigue strength evaluation of self-piercing riveted Al-5052 joints under different specimen configurations. Int J Fatigue 80:58–68
23. Zhao L, He X, Xing B, Lu Y, Gu F, Ball A (2015) Influence of sheet thickness on fatigue behavior and fretting of self-piercing riveted joints in aluminum alloy 5052. Mater Des 87:1010–1017
24. Xing B, He X, Zeng K, Wang Y (2014) Mechanical properties of self-piercing riveted joints in aluminum alloy 5052. Int J Adv Manuf Technol 75:351–361
25. Huang L, Shi Y, Guo H, Su X (2016) Fatigue behavior and life prediction of self-piercing riveted joint. Int J Fatigue 88: 96–110
26. Mori K, Abe Y, Kato T (2012) Mechanism of superiority of fatigue strength for aluminium alloy sheets joined by mechanical clinching and self-pierce riveting. J Mater Process Technol 212:1900–1905
27. ZM S, Lin PC, Lai WJ, Pan J (2014) Fatigue analyses of self-piercing rivets and clinch joints in lap-shear specimens of aluminum sheets. Int J Fatigue 72:53–65
28. Xing B, He X, Wang Y, Yang H, Deng C (2015) Study of mechanical properties for copper alloy H62 sheets joined by self-piercing riveting and clinching. J Mater Process Technol 216:28–36
29. Kato K, Okamoto M, Yasuhara T (2001) Method of joining sheets by using new type rivets. J Mater Process Technol 111:198–203
30. Huang Z, Fan K, Yao Q, Lai J (2011) Numerical simulation and experimental analysis of riveting with pipe rivet. Adv Sci Lett 4: 686–690

31. Huang Z, Xue S, Lai J, Xia L, Zhan J (2014) Self-piercing riveting with inner flange pipe rivet. Procedia Eng 81:2042–2047
32. Huang ZC, Yao QH, Jiang N, Zhou ZJ (2009) Numerical simulation and experiment of self-piercing riveting with solid rivet joining multi-layer aluminum sheets. Mater Sci Forum 628-629:641–646
33. Sheng ZQ, Shivpuri R (2006) A hybrid process for forming thin-walled magnesium parts. Mater Sci Eng A 428:180–187
34. Hatanaka N, Yamaguchi K, Takakura N (2003) Finite element simulation of the shearing mechanism in the blanking of sheet metal. J Mater Process Technol 139:64–70
35. Chen DC, Syu SK, CH W, Lin SK (2007) Investigation into cold extrusion of aluminum billets using three-dimensional finite element method. J Mater Process Technol 192–193:188–193
36. Abe Y, Kato T, Mori K (2006) Joinability of aluminium alloy and mild steel sheets by self piercing rivet. J Mater Process Technol 177:417–421
37. Carandente M, Dashwood RJ, Masters IG, Han L (2016) Improvements in numerical simulation of the SPR process using a thermo-mechanical finite element analysis. J Mater Process Technol 236:148–161